NANO · MICRO small
www.small-journal.com

Correlated Study of Material Interaction Between Capillary Printed Eutectic Gallium Alloys and Gold Electrodes

*Navid Hussain, Torsten Scherer, Chittaranjan Das, Janis Heuer, Rafaela Debastiani, Peter Gumbsch, Jasmin Aghassi-Hagmann, and Michael Hirtz**

Liquid metals (LMs) play a growing role in flexible electronics and connected applications. Here, LMs come into direct contact with metal electrodes thus allowing for corrosion and additional alloying, potentially compromising device stability. Nevertheless, comprehensive studies on the interfacial interaction of the materials are still sparse. Therefore, a correlated material interaction study of capillary-printed Galinstan (eutetic alloy of Ga/In/Sn) with gold surfaces and electrodes is conducted. Comprehensive application of optical microscopy, vertical scanning interferometry, scanning electron microscopy/spectroscopy, x-ray photon spectroscopy, and atomic force microscopy allow for an in depth characterization of the spreading process of LM lines on gold films, revealing the differential spread of the different LM components and the formation of intermetallic nanostructures on the surface of the surrounding gold film. A model for the growth process based on the penetration of LM along the gold film grain boundaries is proposed based on the obtained time-dependent characterization. The distribution of gold, Galinstan, and intermetallic phases in a gold wire dipped into LM is observed using X-ray nano tomography as a complementary view on the internal nanostructure. Finally, resistance measurements on LM lines connecting gold electrodes over time allow to estimate the influence on the material interaction on electronic applications.

1. Introduction

Several advances in stretchable and flexible materials have transformed the concept of flexible electronics from science fiction into a reality, offering a wide range of practical next-generation applications such as solar power generating curtains, electronic skin, and circuits in contact lenses.[1–3] Regarding stretchable materials, gallium-based eutectic liquid metal (LM) alloys have shown broad prospects for flexible and stretchable electronics where system architecture requires bending, rolling, folding, twisting, stretching, and conforming onto irregular shapes. As its name suggests, LM remains in the liquid phase at or even below room temperature (based on the composition). Aside from their excellent liquidity, gallium eutectic LMs are also highly electrically and thermally conductive, with very low vapor pressure, low toxicity, and good biocompatibility.[4,5]

As of these excellent properties, LMs found diverse applications, such as proximity sensors,[6] sensors for strain,[7,8] temperature,[9–11] and acceleration,[10] and other flexible sensors,[12] flexible antennas,[8,12] self-healing interconnects,[13] stretchable wireless power transfer devices,[14] stretchable electromagnetic actuators,[15] stretchable loudspeakers,[16] stretchable interconnects, wires and electronic components,[17,18] devices to integrate light-emitting diodes (LEDs),[10,19] printed diodes and transistors,[17] flexible display devices,[20] flexible solar cells,[21] heat dissipation devices,[22] stretchable thermoelectric generators,[23] e-skin,[24] wearable electronics and biological prosthetic devices,[9,11] wireless monitoring,[25] health monitoring,[6,18] eye-movement tracking,[26] neural microelectrode array,[27] and implantable and epidermal electronics.[27,28]

N. Hussain, T. Scherer, R. Debastiani, P. Gumbsch, J. Aghassi-Hagmann, M. Hirtz
Institute of Nanotechnology (INT)
Karlsruhe Institute of Technology (KIT)
Hermann-von-Helmholtz-Platz 1
76344 Eggenstein-Leopoldshafen, Germany
E-mail: michael.hirtz@kit.edu

The ORCID identification number(s) for the author(s) of this article can be found under https://doi.org/10.1002/smll.202202987.

DOI: 10.1002/smll.202202987

N. Hussain, T. Scherer, R. Debastiani, M. Hirtz
Karlsruhe Nano Micro Facility (KNMFi)
Karlsruhe Institute of Technology (KIT)
Hermann-von-Helmholtz-Platz 1, 76344 Eggenstein-Leopoldshafen, Germany
C. Das
Institute of Applied Materials (IAM-ESS)
Karlsruhe Institute of Technology (KIT)
Hermann-von-Helmholtz-Platz 1, 76344 Eggenstein-Leopoldshafen, Germany
J. Heuer
Institute of Microstructure Technology (IMT)
Karlsruhe Institute of Technology (KIT)
Hermann-von-Helmholtz-Platz 1, 76344 Eggenstein-Leopoldshafen, Germany
P. Gumbsch
Fraunhofer Institute for Mechanics of Materials IWM
Wöhlerstr. 11, 79108 Freiburg, Germany

Most of these flexible electronic devices also include interfaces between solid metal components and LMs, which might critically impact the device's overall functioning. Gallium and gallium alloys are very reactive with some metals such as Al, Au, and Ag, even at room temperature, and they are capable of diffusing into the grain boundaries of these solid metals. It is possible that this penetration can lead to a significant change to the mechanical or electrical properties and these contacts need to be studied as current knowledge is limited here. In their study on capillary printed EGaIn, Park et al. have found ohmic behavior for EGaIn forming electrical connections between pads of three different metals Au, Cu, and Ag. They used two different modes of generating the LM lines, (I) direct-write, where the lines are written directly from one pad to the other thus, the LM interfaces directly to the metal pads, and (II) reconfiguration, where a line is written on glass first and then lifted and laid over the metal pads, which leads to a formation of a thin oxide layer in between the LM and the metal pads. While the oxide layer is thin enough to only cause negligible raise in resistance itself, it changes the interaction between LM and solid metal pads. For the direct-write lines, resistance increased three times after 7 h, while for the reconfigured, oxide-interfacing lines even after 7 days no significant change was observed.[19] Sato et al. also studied contact resistance between Galinstan and a Cu film. A vacuum-induced reduction in the oxide layer's effect has been demonstrated to reduce contact resistance up to 90% compared to the case where the Cu film was placed on a Galinstan surface with an interfacial oxide layer in between. Here, the formation of $CuGa_2$ alloy at the interface to the Cu film was monitored via energy-dispersive X-ray spectroscopy (EDS) and X-ray diffraction (XRD) over time.[29] Recently, the intermetallic wetting of EGaIn on gold was even used for patterning in a neat transfer process for 3D flexible electronic circuitry.[30]

Arguably gold is the most important industrial metal in the manufacture of electronics commonly used as electrodes and connectors, which is a highly efficient conductor and usually remains corrosion-free and stable (other than with LMs). Unfortunately, no comprehensive chemical study of the interaction of LMs with gold is reported yet. The penetration of GaIn alloys into gold electrodes might affect the performance of electronic devices after a certain time. Thus, quantifying these processes is crucial for managing their impact on a device and a critical step to bring devices from lab to commercial and daily life.

In this paper, we have examined the interaction of Galinstan with solid gold surfaces by using vertical scanning interferometry (VSI), EDX/EDS, X-ray photoelectron spectroscopy (XPS), XRD, atomic force microscopy (AFM), and X-ray nano computed tomography (nanoCT). Additionally, we have explored the electrical properties of Galinstan resistors directly printed between gold pads.

2. Results and Discussions

2.1. Printing Method and LM Example Structures

As described in our previous report, Galinstan resistors were fabricated by capillary printing with a customized nanolithography system on laser-ablated Au pads.[17] A five-axis stage is used with automatic movement in the *x*-, *y*-, and *z*-axes, as well as two tilting axes in the *x*–*y*-plane. A glass capillary mounted on a static holder, an ink reservoir stored in a syringe, and a pump to transfer ink constitute the LM writing component. The capillaries with long tapers (around 9–15 mm) and small tips (about 3 μm) were prepared using a pipette puller at appropriate operating parameters. Then, a smooth and continuous motion is used to push against the glass capillary and score it at the right point to obtain the desired aperture size, typically around 40 μm.

As the glass capillary is mounted, LM is filled and extruded in the glass capillary, the syringe pump's flow rate is adjusted to ensure that a continuous deposition is formed and no droplets are formed on the tip of the glass capillary. After the LM was brought to the glass capillary tip, the flow rate was kept low enough to hold the LM at the tip, and then the tip should be brought close to the substrate to make contact. The LM is deposited on the substrate via glass capillaries close to the moving target substrate during the whole printing process. With the help of the syringe pump, the LM flow rate is controlled, while at the same time, the glass substrate mounted on the stage is moved at a controlled speed under contact with a stationary glass capillary held at close vicinity. Once the desired pattern has been achieved, the capillary tip is moved away from the substrate. Several factors affect the dimensions of written patterns, including the inner diameter of the capillary and the size of the opening at the capillary tip. It is possible to increase the height or width of patterned lines by printing with a larger diameter tip or by printing two or more lines next to each other or on top of each other.

In total, five kinds of samples were prepared (Figure S2, Supporting Information) with this printing technique which included two types of resistors, where LM lines were printed in between and over gold electrodes on a glass substrate, and three samples were printed with lines of LM on homogeneously Au-coated glass substrates to measure gallium and indium spreading behavior on gold surfaces. The printed resistors were characterized for resistance with respect to time in a probe station (**Figure 1**a). One of the samples with homogeneous Au-film was encapsulated with PMMA, to study the influence on gallium and indium penetration into the gold surface, while the two others remained uncovered for different correlative measurements. Figure 1b presents a scanning electron microscopy (SEM) and VSI overlay of a LM line structure on a homogenously Au-coated sample 14 days after printing, showing Ga and In widely spread out around the Galinstan line.

2.2. Galinstan–Gold Interaction Correlated Characterization with EDS and VSLI

Ga and In can penetrate from LMs into solid gold along grain boundaries due to stress (then the process is called liquid metal embrittlement (LME)) and a thermodynamic driving force that reduces the interfacial energy (then referred to as grain boundary penetration (GBP)), detailed discussions on these models can be found in the literature.[31–33] The spread rate for the formation of intermetallic nanostructures can be challenging to measure

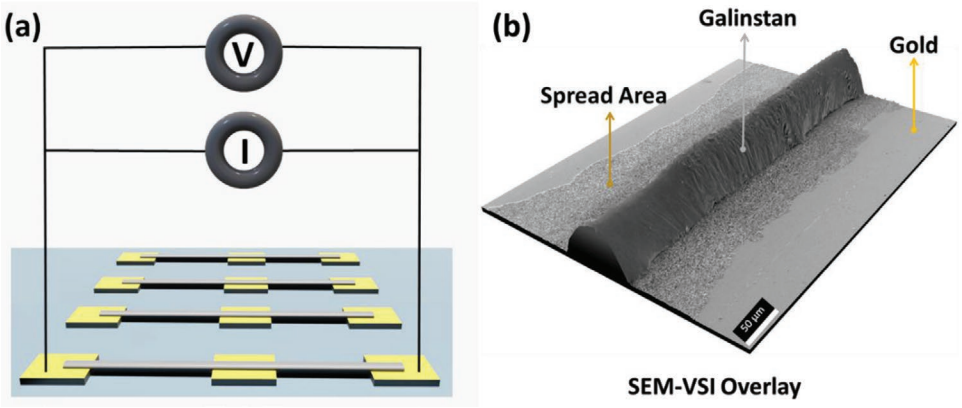

Figure 1. Scheme of Au/liquid metal (LM) setup. a) Conductivity measurement setup based upon 2-point probe system. b) Scanning electron microscopy (SEM) and vertical scanning interferometry (VSI) overlay of printed LM line, see also Figure S1 (Supporting Information).

with one method, so a correlated characterization approach is applied here that combines VSI with EDS and SEM to assess the physical topography and chemical mapping (**Figure 2**a). This correlated characterization provides a comprehensive quantitative description of Ga-In diffusion and formation of intermetallic nanostructures on the surface and underneath and can relate precisely centimeters to nanometer-scale surface topographic measurements. By VSI, structural spread rates can be quantified at a nanometer-scale vertical resolution based on their topographical evolution. The EDS mapping provides additional information about the elemental/chemical spread. Over a timescale of several days, multiple surface maps were obtained and spread rates extracted by subtracting them from each other. The spread distances from the Galinstan line are shown in Figure 2b.

For this correlated characterization, we have prepared two samples on gold surfaces. The first sample was explored with EDS 4 h after the sample preparation. The sample was also studied by VSI subsequently, which show spread for the initial 30 h was around (32.97 ± 3.59) µm, translating into a spread rate of around 1.1 µm h^{-1}. The same area of the sample was followed up for up to 28 days after printing. For the time period 30 to 144 h (day 6) a spread of (34.34 ± 3.30) µm, respectively, a spread rate of 0.3 µm h^{-1} was observed. Assuming and underlying free-space diffusion process through the gold film bulk,[34] the spread S dependence on the spreading time t can be fitted as $S(t) = (5 \pm 0.63)\sqrt{t}$, with an accompanying leveling off spread rate over time. While microscopic penetration as measured in similar systems can be substantially higher

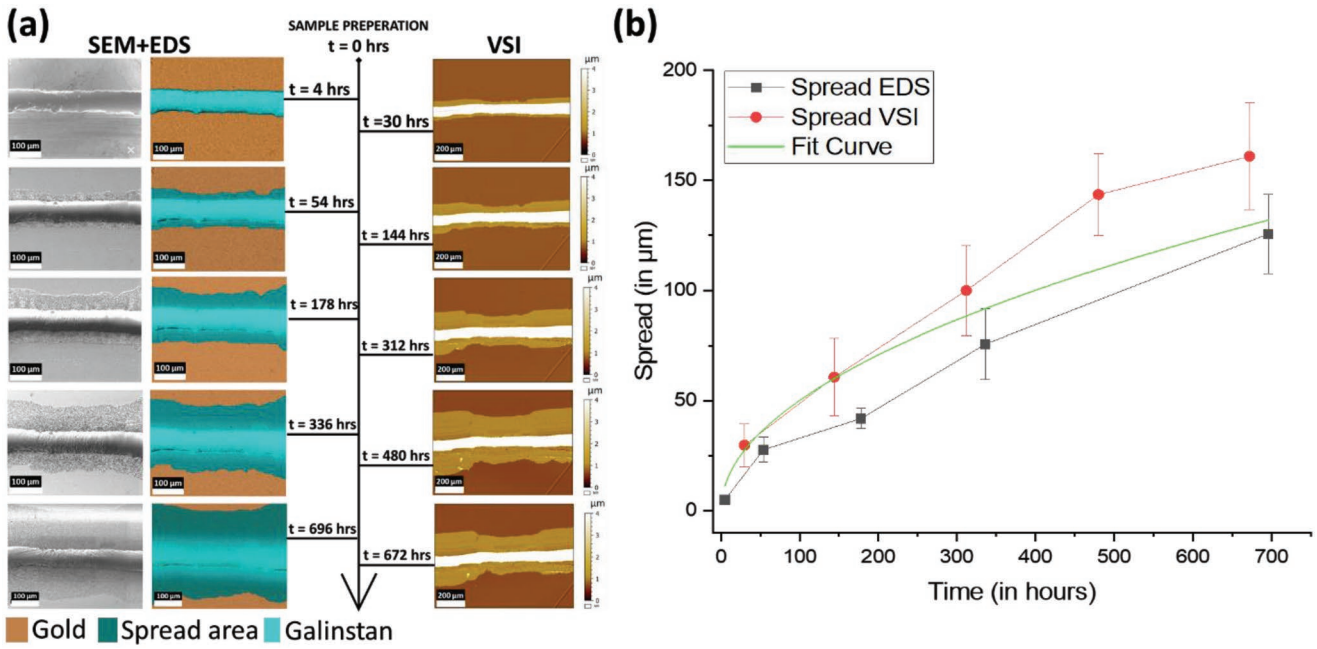

Figure 2. Galinstan spread correlated study with scanning electron microscopy (SEM) + energy-dispersive X-ray spectroscopy (EDS), and vertical scanning interferometry (VSI). a) SEM, EDS, and VSI for the sample with respect to time. b) Spread distances from the Galinstan line. Fitting the spread S dependence of time t assuming free-space diffusion process[34] results in $S(t) = (5 \pm 0.63)\sqrt{t}$.

(e.g., Ga penetration into Al, where in-situ TEM measurements revealed speeds varying between 0.01 to 12.2 μm s^{-1} along the grain boundaries),[35] it must be taken into account that the macroscopic process observed here is result of penetration along the randomly oriented grain boundaries, thus expected to result in a much slower propagation. Compared to the few reports on macroscopic spread (e.g., estimated by us from published optical microscopy images for EGaIn on Ag electrodes to ≈1.5 μm h^{-1})[36] the results seem in line with general expectations for such system. Furthermore, the kinetics of GBP will be influenced by the way of preparation of the metal film, grain boundary type and structure, grain size, mechanical stress, and temperature.[37] Interestingly, the penetration of Ga into grain boundaries can also influence the mobility of the grain boundaries itself, as reported for Ga/Al systems.[38]

Figure 3 shows additional SEM imaging and corresponding EDS maps conducted 4 h after the printing of the LM line. These clearly reveal the formation of intermetallic nanostructures in the spread area around the Galinstan line. Figure 3a shows the grain-like texture of the resulting product at an angle, with the Galinstan line in the background. Figure 3b shows the apparent band of intermetallic nanostructures in the spreading region in top view.

Corresponding EDS maps (Figure 3c) show that Ga and In start spreading into the gold surface immediately on contact. Sn penetration is not seen in initial EDS maps, and only later EDS maps after 1 week (Figures S3–S7, Supporting Information) show slight signals of Sn appearing on the gold surface near the Galinstan line. The differential behavior in penetration speed for Ga, In, and Sn is similar to observations in LM/Zinc systems.[39] The formation of the intermetallic nanostructures becomes visible even to the naked eye after enough time has passed. Here, a striking change in color from the grey/silver appearance of Galinstan to gray/blue color shades can be observed (Figure S8, Supporting Information). This indicates the formation of blue gold, an alloy of gold and either Ga or In. It is reported, that these intermetallic compounds form at 46 wt% Au for $AuIn_2$, and 58.5 wt% Au for $AuGa_2$, respectively.[40,41] Considering the Au–Ga and Au–In phase diagrams, we can observe that there are multiple intermetallic phases, most of which are stable at and below room temperature,[42,43] thus the amount of gold will determine the stoichiometry and phase formation of the resulting nanostructures. Clarysse et al. have reported that regarding Au–Ga systems, small amounts of Ga-amide introduced in Au nanocrystals might result in fcc Ga-doped Au nanocrystals, while proportionally more significant quantities of Ga precursor lead to the conversion of Au seeds to various intermetallic phases including hexagonal Au_7Ga_2, orthorhombic AuGa, and cubic $AuGa_2$.[44] So, the nanostructures seen in the SEM image in Figure 3a, might chemically constitute of a mix of all of those different phases. To clarify the composition of the intermetallic structures, XRD was performed on the sample seen in Figure S8 (Supporting Information). The results taken together with EDS and the notion of formation of energetically favorable intermetallic phases in similar systems[45,46] suggest predominantly $AuGa_2$ in the intermetallic region (Figure S9, Supporting Information).

As a complement to the EDS measurements, the more surface sensitive method of XPS was performed on a sample with a LM line on a homogeneously Au-coated substrate. The spreading of Galinstan on the Au surface was studied by XPS over the period of 120 days (**Figure 4**).

The spectral mapping of spin-orbit splitted Au4f, Ga2p, In3d, and Sn3d core level spectra collected across the LM line on the Au substrate is shown in Figure 4a. The color code blue to red in the map shows the change in intensity of the spectra from lower to higher in the *Y*-axis. While in the *X*-axis, the highest intensity represents the binding energy of the core level spectra. The core-level binding energy of $Au4f_{7/2}$ is 84.2 eV,[47] while for $Ga2p_{3/2}$, $In3d_{5/2}$, and $Sn3d_{5/2}$, it is at 1118.66, 484.90, and

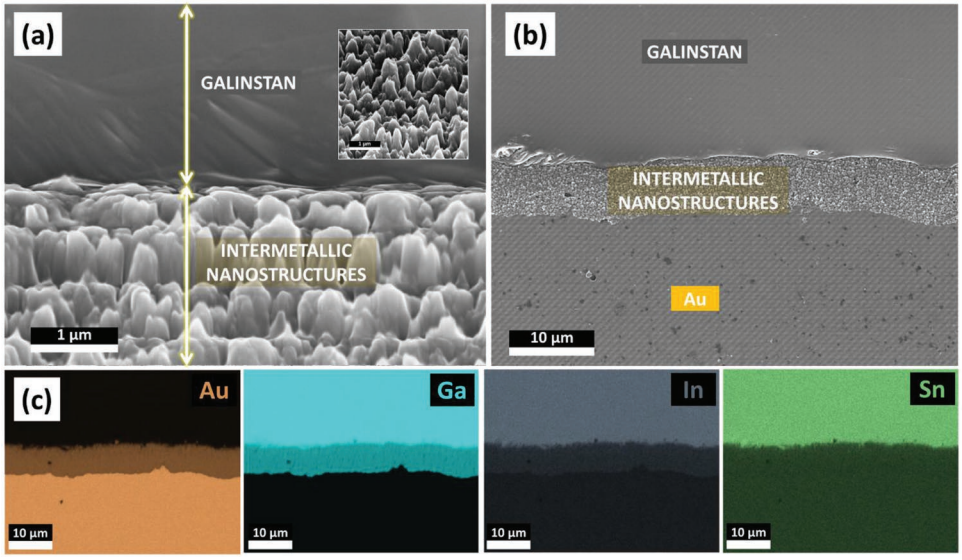

Figure 3. Intermetallic nanostructures formation in Galinstan–gold. a) Scanning electron microscopy (SEM) image at 60° angle (closed view in inset), scale bar: 1 μm. b) SEM image shows an apparent border between the intermetallic nanostructures products and the bare gold surface just after 4 h of printing Galinstan on the Gold surface. c) Energy-dispersive X-ray spectroscopy (EDS) map edge of Galinstan line printed on the gold surface, acquired at 10 kV, 120 pA, WD = 5 mm.

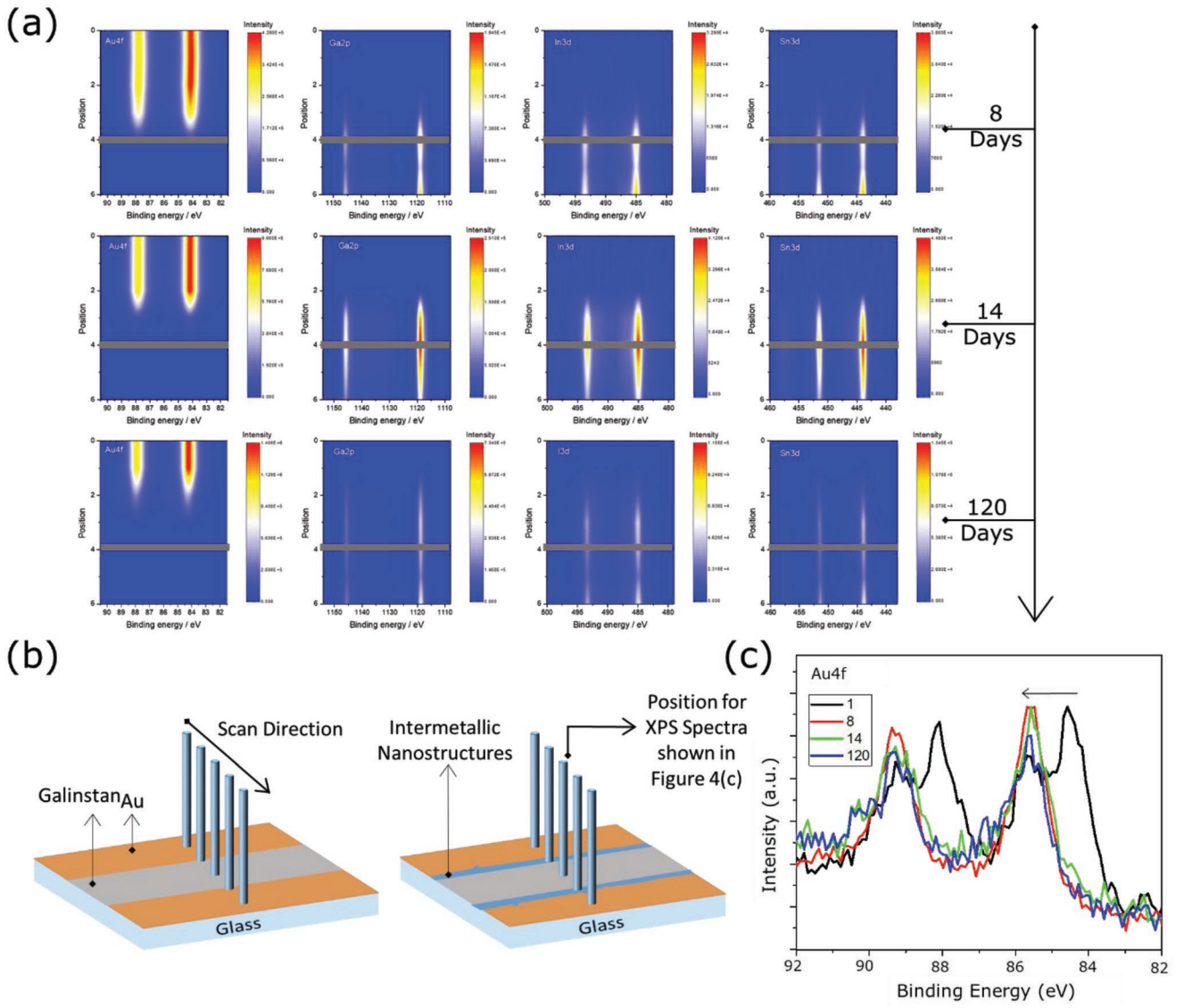

Figure 4. Line scan on a liquid metal (LM) line on a homogeneously Au-coated substrate at 8, 14, and 120 days after printing. a) Core level maps of Au4f, Ga2p, In3d, and Sn3d. The map's color code from blue to red is the lowest to highest intensity of the peak along the *Y*-axis. Point 4 (dark gray line), shows the starting point of the LM line. b) Scheme on the sample and scan positions. c) High-resolution core-level spectra of Au4f orbital for a LM line (at position marked in (b)) on Au for fresh, 8, 14, and 120 days after deposition.

443.90 eV, respectively, corresponding to the metallic gold and the LM components Ga, In, and Sn.[48] However, the binding energy of Ga2p shows the Galinstan is already oxidized after 8 days of film deposition.[17] The Au4f map on the 8th day shows the intensity of spectra has the lowest intensity at around measurement point 4, which is the point when the line scan reaches the edge of the LM line. Around this position, the Ga2p, In3d, and Sn3d peak intensities start to increase, showing steps between Au and the LM. Comparing the Au map from the 8th, 14th, and 120th day, it can be seen that the position of the lowest intensity moved from 4 to 2. Similarly, the Ga2p, In3d, and Sn3d intensities move toward position 2 and beyond that point over the time from the 8th day to the 120th day. The movement of the spectral intensity of Au and LM opposite to each other on the map shows the movement of Ga and In in Gold surface and intermetallic nanostructure formation, which is confirming the observations by the other methods.

Figure 4c shows the Au4f spectra for a point in the center of the LM line on Au (as depicted in Figure 4b) for the 1st, 8th, 14th, and 120th day after sample preparation. On the first day, the $Au4f_{7/2}$ has two peaks at 84.5 and 85.7 eV corresponding to the In–Au and Au–Ga eutectic.[49,50] From the first-day spectra, it is evident that some Au migrated to the surface of the LM film, forming a eutectic alloy with the LM. With the increase of time, the $Au4f_{7/2}$ has only one peak at 85.7, indicating the Au mixes completely with the LM to form a eutectic. The combined observation of Figure 4a,c shows that the LM spreads into the Au film over the time, but also some Au migrated into the LM, forming a eutectic. Figure S10 (Supporting Information) shows the Ga3d, In3d, and Sn3d core level spectra collected

on the 1st, 8th, 14th, and 120th day. In Ga3d core level spectra the peak at around 20.8 eV and in Sn3d core level spectra the shoulder at around 487.0 eV show that the surface is oxidized with the formation of Ga_2O_3 and SnOx on the surface of the LM, while the In3d position does not change over time. This is in agreement to our previous work, where we calculated the thickness of Ga_2O_3 on Galinstan over time.[17] The oxide layer can be removed by HCl vapor treatment (Figure S11, Supporting Information), but stable $GaCl_3$ hindered further XPS characterization of the intermetallic structures.[51]

Revisiting the sample in optical microscopy after several cycles of correlative measurements revealed another interesting phenomenon (**Figure 5**).

Here, the intermetallic nanostructures show up in bands of slightly different reflectivity, as can be seen in the optical microscopy image of the spread area (Figure 5a). The contrast change does not indicate a chemical difference of the bands in regard to Ga, In, Au, and Sn contents, as EDS shows homogeneous chemical signal for the spread area at all aging stages (Figures S2–S6, Supporting Information). Therefore, we suspected different morphologies of the spread areas in the different bands, and a more detailed microstructural analysis with high magnification SEM and roughness measurement with AFM were implemented. SEM imaging at a 60° angle and AFM at the different bands (P1 to P6) show the general topography in AFM and corresponding SEM images (Figure 5c and Figure S12, Supporting Information). Both show pit and heightened hill structures in close vicinity uniformly dispersed throughout the surface. Scans of the complete areas reveal that the Au surface is fully covered with the intermetallic nanostructures, with no sign of any bare Au surface in between. All of the positions in the sample show similar hill structures in regard to size and height, which can be clearly observed in profile lines extraction from the AFM images (Figure 5d). In addition to the topography, a roughness analysis was performed to provide additional information about the texture. Both, the arithmetical mean deviation roughness (Sa) and the root mean square roughness (Sq) as measured by AFM present a low overall roughness varying from 42 to 55 nm (Sa) and 52 to 68 nm (Sq), respectively, with maximum heights of the

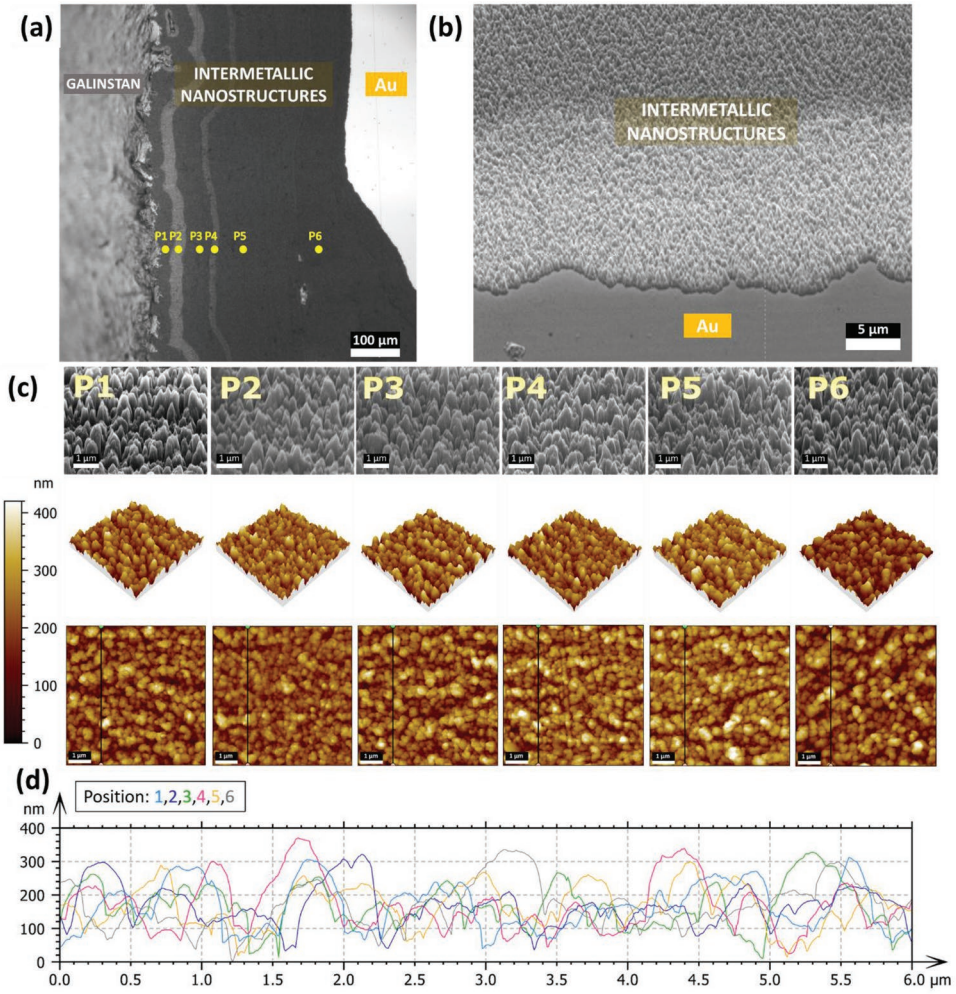

Figure 5. Correlated scanning electron microscopy (SEM) and atomic force microscopy (AFM) measurements on liquid metal (LM) spread. a) Optical microscopy image showing different shades of intermetallic nanostructure products. b) SEM image of the edge of the intermetallic nanostructures band with the adjacent bare gold surface. c) SEM imaging at a 60° angle (scale bar 1 µm) and corresponding AFM images for different positions. d) Profile extraction from AFM images of positions.

Table 1. Surface roughness for the positions in shades where the roughness average (Sa) represents the mean height on the surface, and the root mean square (Sq) indicates the standard deviation (SD) from the mean height.

Position	Mean Height Sa [nm]	Root Mean Square Height Sq [nm]	Maximum Height Sz [nm]
1	53.2	65.1	429.1
2	41.7	52.2	401.8
3	54.7	67.0	432.6
4	50.7	63.4	464.6
5	52.4	64.6	443.5
6	54.7	67.8	486.1

intermetallic structures varying from 400 to 500 nm for the different bands (**Table 1**).

As even small changes in surface roughness and morphology can introduce substantial changes in reflectance of surfaces,[52] the differences between the bands seem sufficient for explaining the observed contrast. Furthermore, the bands can be correlated with cycles of vacuum (during XPS/EDS) and in air spreading, with the width of bands increasing with longer measuring or aging times (Figure S13, Supporting Information), indicating that the source of the different roughness could be different mechanical stresses during vacuum exposure and storage at ambient pressure.

Finally, another line-printed sample was encapsulated with PMMA to look for factors affecting the spread of Galinstan on gold. Here, optical microscopy images were captured with respect to time (Figure S14, Supporting Information). The PMMA encapsulation cannot prohibit LM spreading, however substantially slows down at least the surface visible outgrowth, probably by mechanical blocking and acting as a stabilizer for the surface. To inspect whether the Au-film gets only alloyed on the surface or also in deeper layers, a focus ion beam (FIB) section was prepared in an area of the intermetallic nanostructures (Figure S15, Supporting Information). Gold and Ga signals fully correlate in the section down to the silicon substrate, thus showing that the complete gold film got consumed by the LM spread.

Additionally, the X-ray nano tomography provided the 3D distribution of the Galinstan, gold, and intermetallic phases after 53 days of dipping a gold wire into Galinstan. **Figure 6** shows a 3D view of the sample in grayscale and color mapped. The composition distribution is retrieved through the differences in the grayscale, with lighter gray corresponding to denser material. The scanned tip of 31 μm^3 has a distribution of ≈48% of intermetallic phases, 35% of Galinstan, 12% of gold, and 5% of oxygen. While the inner structure is mostly intermetallic phases and gold, Galinstan is distributed in the more external layers and oxygen forms a thin layer on the sample surface (Figure S16 and Video S1, Supporting Information).

Taking together the results so far, a growing mechanism for the intermetallic nanostructures can be proposed based on the penetration of Ga and In from the LM into the gold surface (**Figure 7**).

In this model, the intermetallic structures are products of Ga and In alloying with Au after diffusion along intergranular cracks produced at grain boundaries of the underlying gold film. Multiple theories exist for crack initiation and LME/GBP based on adsorption or diffusion–penetration of LM atoms on solid metal surfaces and weakening of interatomic bonds.[31–33] Microvoid coalescence (MVC) and the dissolutions-condensation mechanism (DCM) are expected to be the reason for intergranular cracking. As the details of cracking, volume changes and the vertical growth of the nanostructures itself will depend on mechanical stresses in the gold and interactions at the surfaces, in this model, it also becomes conceivable why slightly different morphologies for the intermetallic structures leading to the band structures in the spread area are formed. They reflect the different pressure regimes under which XPS and EDS, and the aging under ambient conditions at atmospheric pressure take place. While the focus in this work is on the time evolution of the Galinstan gold systems, some explorative experiments in regard to temperature and humidity were performed as it is known for Ga/Al systems that raising temperature can highly increase Ga penetration into grain boundaries.[37] For this, sets of samples were kept for 18 h under different temperature and humidity conditions and spread was measured afterwards (Table S1, Supporting Information). This revealed that the influence of humidity seems negligible, but

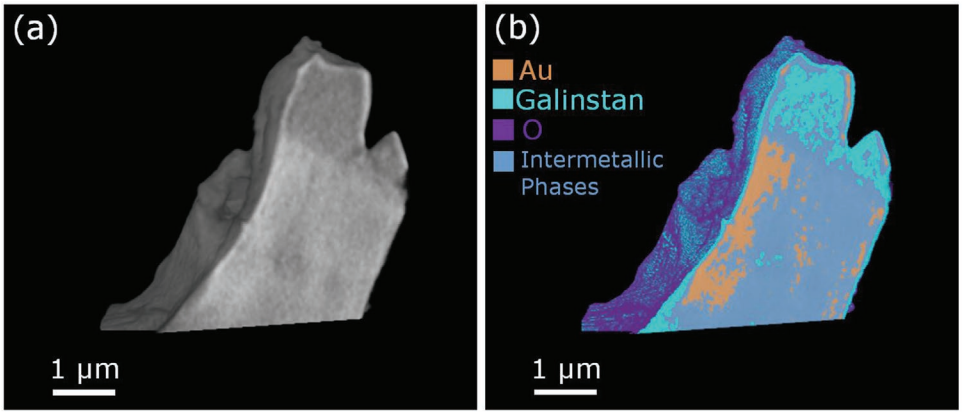

Figure 6. Volumetric reconstruction of a nano computed tomography (nanoCT) scan performed 53 days after dipping a gold wire into the Galinstan in a) grayscale and b) color mapped.

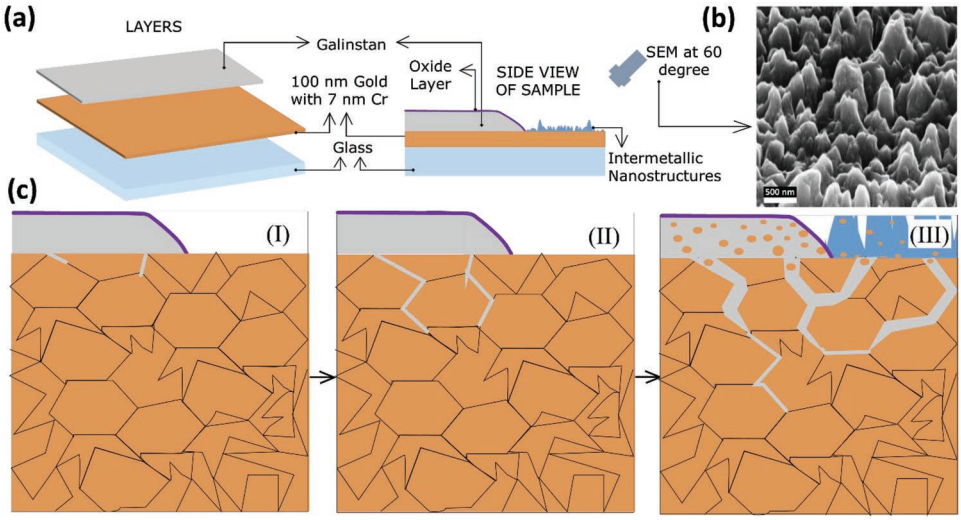

Figure 7. Model of intermetallic nanostructure formation. a) Schematic of the sample setup. b) Scanning electron microscopy (SEM) image of the intermetallic nanostructures at 60° view angle. c) Proposed growing mechanism for the intermetallic nanostructures. I) Crack initiation, II) grain boundary penetration, and III) intermetallic nanostructure formation. Color representations are—light blue: glass, orange: gold, gray: Galinstan, blue: intermetallic nanostructures, and purple: oxide layer.

heating the substrates to elevated temperatures of 50 °C and 100 °C substantially increases spread in particular for thicker line structures.

2.3. LM Interconnects and Resistors

To investigate the effect of time aging on the electrical properties of Galinstan–gold contacts, we measured the total resistance between the printed Galinstan pattern in between two gold pads. For this, printed (38.38 ± 2.35) µm wide Galinstan lines (**Figure 8**) connecting two gold pads located at 500 µm for sample 1 and 1620 µm for sample 2 (including 420 µm of the middle gold pad). The resistance between the pads was measured using two probes for the samples for freshly prepared samples after 7 days, 1 month, and 2 months of interval. Optical microscope images were also captured for the same intervals. As the optical microscope images show in Figure 8a, the Galinstan starts reacting with a gold pad immediately after the printing, and after 2 months, the gold pads are entirely covered.

The resistance measured using two probes increased with respect to air aging. The resistance for directly printed Galinstan resistors between two gold pads was (8.11 ± 4.77), (6.47 ± 1.32), (9.56 ± 2.68), and (11.77 ± 5.33) Ω for fresh, after 7 days, 1 month and 2 months ageing, respectively. On the other hand, for sample 2, it was found to be (8.05 ± 3.10), (6.99 ± 1.36), (12.45 ± 3.36), and (20.01 ± 7.38) Ω for the same time intervals, respectively. Both of the data were measured for an average of 10 samples. Overall, there is only a slight difference in total resistance over time. However, there is a higher increase for the sample 2 were the LM line was traversing a 420 µm additional gold pad in contrast to the direct connection of electrodes in

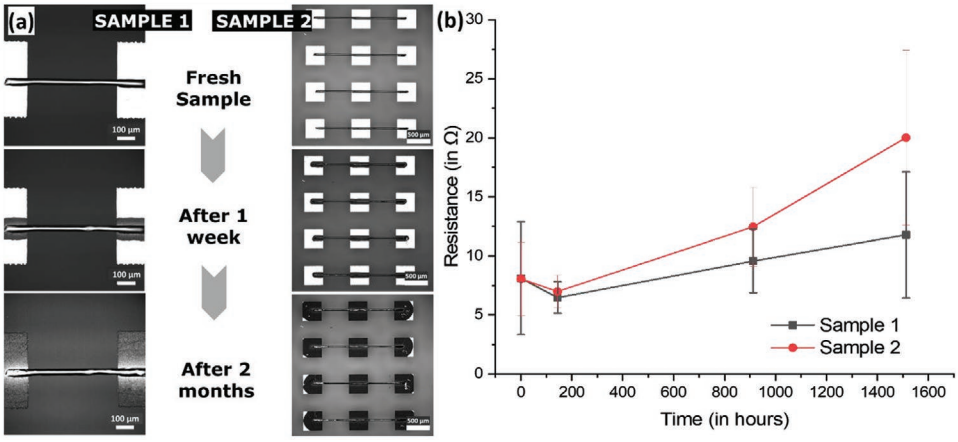

Figure 8. Printed resistors. a) Printed Galinstan lines between two gold pads (average width: 38.38 ± 2.35 µm), the distance between two gold pads 500 µm for sample 1 and 1620 µm for sample 2 (including 420 µm of the middle gold pad). b) Resistance studies with respect to time for two types of printed resistors.

sample 1. This could indicate an additional change in LM composition and internal structure over the middle part of the connection in sample 2, were it is in direct contact with the gold pad. Here, Au can penetrate back into the LM line itself (Figure S17, Supporting Information), potentially raising the LM lines' resistance as of the introduced phase boundaries and localized composition changes, as, e.g., also observed in Fe loaded LMs.[53]

3. Conclusion

In summary, we have studied a time-dependent spread of the LM Galinstan on gold surfaces in a correlated characterization, including spatially resolved EDS maps, VSI maps that quantify spread rate into the Au film, and SEM/AFM images for morphology and roughness analysis. The characterization revealed a growth of granular intermetallic nanostructures of Ga/In/Au alloys around the printed LM lines and allowed to develop a microscopic model of spreading and nanostructure growth. The 3D volume distribution of Galinstan, gold, and intermetallic alloys was obtained using X-ray nano tomography. These demonstrated methods can also help to predict a lifetime for LM printed devices.[54] EDS and SEM images also show that Ga–In penetration into the grain boundary network starts immediately on Galinstan deposition, and the spread slows over time consistent with a diffusion process. For the printed Galinstan lines, it was observed that Ga and In penetrate much faster and to a larger extend into the gold film in comparison to Sn. While the different microscopy and spectroscopy methods show a clear reconfiguration of the materials, the electrical characterization of LM lines printed Galinstan between gold electrodes did show only a slight increase in resistance over time, which gives a positive prospect for stable devices in regard to electronic applications of LM.

4. Experimental Section

Materials: Galinstan, composed of 68% gallium, 21% indium, and 11% tin by weight, was acquired from Strategic Elements, Germany. 2-Propanol (≥99,8%, p.a.) and Chloroform (p.a.) obtained from CarlRoth and VWR respectively, PMMA dissolved in Anisol was obtained from Micro Chem. All materials were used as received.

Preparation of Substrates: Glass coverslips (from VWR Germany) were cleaned with chloroform, 2-propanol, and deionized water, then dried with nitrogen. At the second step, substrates were cleaned in an ATTO B plasma-cleaner (Diener electronic GmbH, Germany) using oxygen plasma (10 sccm O2, 0.2 mbar, 100 W, 2 min). For improved adhesion, the glass substrates were coated firstly with a 7 nm Cr layer (adhesion layer) and 100 nm Au on top. The microcontact pads were formed by laser ablation with a TRUMPF TruMicro 5000 laser system. Following laser structuring of the Au structures, the substrates were rinsed with 2-propanol and deionized water, dried with nitrogen steam. These Au micropatterns serve as contact pads for the printed Galinstan interconnects.

Preparation of Nozzles: Preparation of glass capillaries with different tips and taper sizes was carried out using a P-1000 micropipette puller system from Sutter Instruments. Warner Instruments' GC120TF-10 glass pipettes were used. They had outer and inner diameters of 1.2 and 0.94 mm, respectively, and a length of 100 mm. The capillaries with long tapers (around 9–15 mm) and small tips (about 3 µm) were prepared and scored for desired tip size of around 40 µm.

Printing Setup: A printing setup, as previously reported, was used for all the direct writing experiments.[17] Direct writing of Galinstan lines was completed using a stationary glass capillary mounted on a modified NLP 2000 nanolithography system (NanoInk, USA), which provides a translation stage that can move in three directions (*X*, *Y*, *Z*) and a microscope to view the printing process from above the sample. The glass capillary used for printing was fitted into a custom holder fabricated in-house in the workshop. LDPE tubing of an inner diameter of 0.1 mm and an outer diameter of 3 mm was used to connect the glass capillary to the syringe pump. Each experiment used Galinstan as ink, injected from the syringe (ink reservoir) into the glass capillary via LDPE tubing at a constant flow rate (around 10 µL min^{-1}), and this flowrate was tuned to ensure a stable pressure (5–100 µL min^{-1}). The glass capillary tip's height was kept constant for the experiment, and the optical microscope was used to observe the tip's interaction with the glass substrate and printing. In order to print, the stage was first moved to the point where the pattern starts. Once the capillary tip had reached the starting position, it was held at a certain height from the substrate according to the tip size. The printing was then initiated by bringing the capillary in contact with the surface (0 µm tip surface distance), and the pre-programmed stage movements were started to form the desired pattern (tip surface distance set to of 3–5 µm and stage moving speed of 1000 µm s^{-1}). Once the pattern is complete, the stage automatically moves down to a safe position, and the glass capillary is separated from the pattern and substrate.

Galinstan Interconnects and Lines Fabrication: Next, the Galinstan interconnects and lines were printed using the customized nanolithography system described above at a writing speed of 1000 µm s^{-1}. All experiments were conducted on freshly cleaned substrates. After printing, interconnects were characterized by optical microscope and by resistance measurements. The printed Galinstan lines were characterized with the techniques discussed in the paper with correlated characterization (EDS, SEM, and VSI). In between measurements, samples were stored in a closed box under ambient lab conditions (≈24 °C, ≈37% r.H., ≈1000 hPa).

Encapsulation of Galinstan Interconnects with PMMA: Printed lines were encapsulated with PMMA (dissolved in Anisol from Micro Chem) using a spin coater at 4000 rpm for 60 s with 10 s ramp up and ramp downtimes. Following the encapsulation, the substrate was heated on a hotplate to 150 °C for 3 min to cure the PMMA. After curing, the lines were characterized with an optical microscope with respect to time.

Optical Imaging Setups: Microscope Images of interconnects and lines were acquired using a Nikon Eclipse 80i upright microscope (Nikon, Japan) equipped with a Nikon DS-Qi2 camera (Nikon, Germany) and a broadband excitation light source (C-HGFIE Intensilight, Nikon). NIS-Elements imaging software was used to evaluate the dimension measurements of interconnects and lines.

Scanning Electron Microscopy Imaging, FIB and Energy-Dispersive X-Ray Spectroscopy: The Zeiss AURIGA 60 FIB/SEM cross-beam system was used for imaging (SEM), while the FIB was used for milling. For milling markers (X) for the correlated study, Ga^+ ions were used at an energy of 30 kV and currents of 1 nA. SEM images were recorded using primary electron energies of 5,10, 20 keV at variable beam currents with in-lens and SESI-detector respectively.

EDS measurements were also done with the same Zeiss Auriga 60 system, using an EDAX Octane Super A detector controlled by EDAX TEAM software. EDS mappings were carried out using 10 kV and 120 pA e-beam conditions and X-ray Lα-signals for Ga, Mz-signals for In and Sn.

X-Ray Diffraction (XRD): XRD was performed on the liquid metal on gold sample as shown in Figure S8 (Supporting Information) at room temperature using a Bruker D8 Advance (Cu Kα1 radiation, $\lambda = 1.54056$ Å).

Vertical Scanning Interferometry (VSI): We performed large-scale (µm-millimeter range) topography measurements with a white light VSI Contour GT-K (Bruker) using 5× magnification (pixel size ≙ 0.75 µm). We processed and analyzed the topography data in MountainsMap (Digital Surf). In particular, we generated an SEM-VSI overlay using the colocalization feature of this software, in which we select identical features in the SEM and VSI image, in this case, FIB inscribed reference crosses.

Atomic Force Microscopy (AFM): For smaller scale topography measurements (nm-µm range), we used an atomic force microscope Dimension Icon (Bruker) in tapping mode with (All-in-One-Al, Budget Sensors Ltd., 65 kHz Resonanz frequency). AFM images for different positions on Galinstan spread area were obtained with NanoScope Analysis software. The AFM data were flattened via a form removal function using a least-squares 7th polynomial. Afterwards, we performed a roughness analysis according to the ISO 25 178 standard.

X-Ray Photoelectron Spectroscopy (XPS): The sample was embedded into one sample holder to maintain the scan position for multiple scans with respect to time. The XPS measurements were done with a Thermofisher K-alpha system. Monochromatic Al- kα X-ray having photon energy 1480.6 eV. The emitted photoelectrons were collected in the analyzer at 90° to the sample's surface. For data analysis, Thermofisher's Avantage software was used.

Electrical Resistivity Measurements: A probe station with an Agilent 4156C semiconductor parameter analyzer with a current detection limit of 30 fA was used to measure resistance. Measurements were completed with voltage sweeps from 0 to 100 mV and a step size of 1 mV; the average of 10 samples was used as a single data point.

NanoCT: A tip with few micrometers of a gold wire dipped briefly into Galinstan (Figure S16, Supporting Information) was scanned 53 days after preparation using the lab-based nanoCT Xradia 810 Ultra. This system uses a semi-monochromated X-ray beam from a Cr anode (energy of 5.4 keV) and a sequence of optics to achieve pixel size of 16 nm within a high resolution field of view setup corresponding to 16 µm. The sample was scanned using high resolution absorption contrast mode, acquiring 701 projections over 180° with an acquisition time of 200 s per projection. Differences in the composition distribution in the specimen are accessed through the difference in the grayscale pixel values, which are directly related to the density of the sample material. The 3D reconstruction of the tomography was performed using the proprietary Zeiss Scout and Scan Reconstructor software, which is based on filtered back projection algorithm. The 3D visualization and manual segmentation were performed using the ORS Dragonfly software (Object Research Systems, Quebec, Canada).[55]

Statistical Analysis: All error bars in graphs and error ranges reported represent one standard deviation (SD) of the reported mean. EDS/VSI images from the same sample positions were used to quantify the spread (Figure 2). In each image, the perpendicular distance of 15 random points at the spread front to the LM line were measured. The fit was done in Origin (OriginLab, USA). For each data point, the resistance was measured for 10 samples (Figure 8). All reported values were calculated from the whole area of the recorded AFM images in MountainsMap (Table 1) (Digital Surf, France).

Supporting Information

Supporting Information is available from the Wiley Online Library or from the author.

Acknowledgements

This work was partly carried out with the support of the Karlsruhe Nano Micro Facility (KNMF, www.knmf.kit.edu), a Helmholtz Research Infrastructure at Karlsruhe Institute of Technology (KIT, www.kit.edu). The Xradia 810 Ultra (nanoCT) core facility was supported (in part) by the 3DMM2O – Cluster of Excellence (EXC-2082/1 – 390761711). R.D., P.G., and J.A. acknowledge the support by the Cluster of Excellence 3DMM2O (EXC_2082/1-390761711) funded by the German Research Council (DFG). M.H. acknowledges the additional support by the Helmholtz Association in the form of a Helmholtz ERC Recognition Award.

Open access funding enabled and organized by Projekt DEAL.

Conflict of Interest

The authors declare no conflict of interest.

Data Availability Statement

The data that support the findings of this study are available from the corresponding author upon reasonable request.

Keywords

Galinstan, liquid metals, printed electrodes, printed electronics, X-Ray nanoCT

Received: May 13, 2022
Revised: July 29, 2022
Published online:

[1] D. Corzo, G. Tostado-Blázquez, D. Baran, *Front. Electron.* **2020**, *1*, 594003.
[2] SunCurtain, https://www.suncurtain.solar/en/the-product/ (accessed: July 2022).
[3] Mojo Lens, https://www.mojo.vision/mojo-lens (accessed: July 2022).
[4] K. Khoshmanesh, S. Tang, J. Y. Zhu, S. Schaefer, A. Mitchell, K. Kalantar-zadeh, M. Dickey, *Lab Chip* **2017**, *17*, 974.
[5] T. Liu, P. Sen, C. J. Kim, *J. Microelectromech. Syst.* **2012**, *21*, 443.
[6] K. Kim, J. Choi, Y. Jeong, I. Cho, M. Kim, S. Kim, Y. Oh, I. Park, *Adv. Healthcare Mater.* **2019**, *8*, 1900978.
[7] X. P. Hao, C. Y. Li, C. W. Zhang, M. Du, Z. Ying, Q. Zheng, Z. L. Wu, *Adv. Funct. Mater.* **2021**, *31*, 2105481.
[8] B. Ma, C. Xu, J. Chi, J. Chen, C. Zhao, H. Liu, *Adv. Funct. Mater.* **2019**, *29*, 1901370.
[9] H. Ota, M. Chao, Y. Gao, E. Wu, L.-C. Tai, K. Chen, Y. Matsuoka, K. Iwai, H. M. Fahad, W. Gao, H. Y. Y. Nyein, L. Lin, A. Javey, *ACS Sens.* **2017**, *2*, 990.
[10] K. B. Ozutemiz, J. Wissman, O. B. Ozdoganlar, C. Majidi, *Adv. Mater. Interfaces* **2018**, *5*, 1701596.
[11] H. Ota, S. Emaminejad, Y. Gao, A. Zhao, E. Wu, S. Challa, K. Chen, H. M. Fahad, A. K. Jha, D. Kiriya, W. Gao, H. Shiraki, K. Morioka, A. R. Ferguson, K. E. Healy, R. W. Davis, A. Javey, *Adv. Mater. Technol.* **2016**, *1*, 1600013.
[12] J. H. So, J. Thelen, A. Qusba, G. J. Hayes, G. Lazzi, M. D. Dickey, *Adv. Funct. Mater.* **2009**, *19*, 3632.
[13] G. Li, X. Wu, D.-W. Lee, *Sens. Actuators, B* **2015**, *221*, 1114.
[14] S. H. Jeong, K. Hjort, Z. Wu, *Sci. Rep.* **2015**, *5*, 8419.
[15] G. Mao, M. Drack, M. Karami-Mosammam, D. Wirthl, T. Stockinger, R. Schwödiauer, M. Kaltenbrunner, *Sci. Adv.* **2020**, *6*, eabc0251.
[16] S. W. Jin, J. Park, S. Y. Hong, H. Park, Y. R. Jeong, J. Park, S.-S. Lee, J. S. Ha, *Sci. Rep.* **2015**, *5*, 11695.
[17] N. Hussain, T. Fu, G. Marques, C. Das, T. Scherer, U. Bog, L. Berner, I. Wacker, R. R. Schröder, J. Aghassi-Hagmann, M. Hirtz, *Adv. Mater. Technol.* **2021**, *6*, 2100650.
[18] G. Li, F. Sun, H. Chen, Y. Jin, A. Zhang, J. Du, *ACS Appl. Mater. Interfaces* **2021**, *13*, 56961.
[19] Y. G. Park, H. S. An, J. Y. Kim, J. U. Park, *Sci. Adv.* **2019**, *5*, eaaw2844.
[20] M. Wang, C. Ma, P. C. Uzabakiriho, X. Chen, Z. Chen, Y. Cheng, Z. Wang, G. Zhao, *ACS Nano* **2021**, *15*, 19364.
[21] K. Chu, B. G. Song, H.-I. Yang, D.-M. Kim, C. S. Lee, M. Park, C.-M. Chung, *Adv. Funct. Mater.* **2018**, *28*, 1800110.

[22] J. Y. Zhu, S.-Y. Tang, K. Khoshmanesh, K. Ghorbani, *ACS Appl. Mater. Interfaces* **2016**, *8*, 2173.
[23] M. Zadan, M. H. Malakooti, C. Majidi, *ACS Appl. Mater. Interfaces* **2020**, *12*, 17921.
[24] U. P. Claver, G. Zhao, *Adv. Eng. Mater.* **2021**, *23*, 2001187.
[25] Y. R. Jeong, J. Kim, Z. Xie, Y. Xue, S. M. Won, G. Lee, S. W. Jin, S. Y. Hong, X. Feng, Y. Huang, J. A. Rogers, J. S. Ha, *NPG Asia Mater* **2017**, *9*, e443.
[26] Z.-N. Zhao, J. Lin, J. Zhang, Y. Yu, B. Yuan, C.-C. Fan, L. Wang, J. Liu, *IEEE Sens. J.* **2018**, *18*, 2592.
[27] R. Guo, J. Liu, *J. Micromech. Microeng.* **2017**, *27*, 104002.
[28] X. Wang, Y. Zhang, R. Guo, H. Wang, B. Yuan, J. Liu, *J. Micromech. Microeng.* **2018**, *28*, 034003.
[29] T. Sato, K. Yamagishi, M. Hashimoto, E. Iwase, *ACS Appl. Mater. Interfaces* **2021**, *13*, 18247.
[30] L. Johnston, J. Yang, J. Han, K. Kalantar-Zadeh, J. Tang, *J. Mater. Chem. C* **2022**, *10*, 921.
[31] J. E. Norkett, M. D. Dickey, V. M. Miller, *Metall. Mater. Trans. A* **2021**, *52*, 2158.
[32] E. E. Glickman, *Metall. Mater. Trans. A* **2011**, *42*, 250.
[33] W. Ludwig, E. Pereiro-López, D. Bellet, *Acta Mater.* **2005**, *53*, 151.
[34] B. Chen, X. Fu, J. Tang, M. Lysevych, H. H. Tan, C. Jagadish, A. H. Zewail, *Proc. Natl. Acad. Sci. U. S. A.* **2017**, *114*, 12876.
[35] R. C. Hugo, R. G. Hoagland, *Acta Mater.* **2000**, *48*, 1949.
[36] Y.-G. Park, H. S. An, J.-Y. Kim, J.-U. Park, *Sci. Adv.* **2019**, *5*, eaaw2844.
[37] H.-S. Nam, D. J. Srolovitz, *Acta Mater.* **2009**, *57*, 1546.
[38] D. A. Molodov, U. Czubayko, G. Gottstein, L. S. Shvindlerman, B. Straumal, W. Gust, *Philos. Mag. Lett.* **1995**, *72*, 361.
[39] N. Tsutsui, H. Koizumi, *Proc. Struct. Integr.* **2018**, *13*, 849.
[40] C. Cretu, E. van der Lingen, *Gold Bull.* **1999**, *32*, 115.
[41] K. E. Saeger, J. Rodies, *Gold Bull.* **1977**, *10*, 10.
[42] J. Wang, Y. J. Liu, L. B. Liu, H. Y. Zhou, Z. P. Jin, *Calphad* **2011**, *35*, 242.
[43] C. Shen, K. Hu, L. Fan, H. Zhang, *J. Phase Equilib. Diffus.* **2021**, *42*, 479.
[44] J. Clarysse, A. Moser, O. Yarema, V. Wood, M. Yarema, *Sci. Adv.* **2021**, *7*, eabg1934.
[45] J. Tang, X. Zhao, J. Li, R. Guo, Y. Zhou, J. Liu, *ACS Appl. Mater. Interfaces* **2017**, *9*, 35977.
[46] J. Tang, S. Lambie, N. Meftahi, A. J. Christofferson, J. Yang, J. Han, M. A. Rahim, M. Mayyas, M. B. Ghasemian, F.-M. Allioux, Z. Cao, T. Daeneke, C. F. McConville, K. G. Steenbergen, R. B. Kaner, S. P. Russo, N. Gaston, K. Kalantar-Zadeh, *Nat. Synth.* **2022**, *1*, 158.
[47] N. H. Turner, A. M. Single, *Surf. Interface Anal.* **1990**, *15*, 215.
[48] F. Scharmann, G. Cherkashinin, V. Breternitz, C. Knedlik, G. Hartung, T. Weber, J. A. Schaefer, *Surf. Interface Anal.* **2004**, *36*, 981.
[49] D. T. Jayne, N. S. Fatemi, V. G. Weizer, *J. Vac. Sci. Technol., A* **1991**, *9*, 1410.
[50] S. C. Ghosh, M. C. Biesinger, R. R. LaPierre, P. Kruse, *J. Appl. Phys.* **2007**, *101*, 114322.
[51] D. Kim, P. Thissen, G. Viner, D. W. Lee, W. Choi, Y. J. Chabal, J. B. Lee, *ACS Appl. Mater. Interfaces* **2013**, *5*, 179.
[52] *Light Scattering and Nanoscale Surface Roughness* (Ed.: A. A. Maradudin), Springer US, Boston, MA **2007**.
[53] R. Guo, X. Sun, B. Yuan, H. Wang, J. Liu, *Adv. Sci.* **2019**, *6*, 1901478.
[54] K. L. Dorsey, N. Lazarus, *Adv. Mater. Technol.* **2021**, *6*, 2001100.
[55] Dragonfly, Object Research Systems, https://www.theobjects.com/index.html (accessed: July 2022).